1 Introduction

The origin of our Solar System can be studied by observations of currently forming protostars in our Galaxy. Tracing the evolution of protostars that will eventually resemble our Sun is fundamental to understand our own origins. Low-mass stars (M ~0.08–1.5 $M_{\odot}$) dominate the star formation in galaxies both in total mass and number (Kroupa 2002, Chabrier 2003). The less numerous high-mass stars ($M \gtrsim 8\ M_{\odot}$) strongly influence the formation of low-mass stars via strong radiation, winds, and injection of heavy elements and are therefore equally important to study (Zinnecker & Yorke 2007, Krumholz et al. 2014).

One of the most interesting aspects of star formation is the scale of material condensation needed to form a star: from about ~10 particles per cm^3 in the interstellar medium, ~10^4 cm^{-3} in molecular clouds, ~10^6 cm^{-3} in dense cores and filaments, to ~10^{24} cm^{-3} in stellar cores (Mottram et al. 2013). The gravitational collapse alone is however too efficient by a factor of ~20 in forming stars compared to the actual observed star formation rates (Leroy et al. 2008, Evans et al. 2009) and must be slowed down by some combination of turbulence, radiation, outflows, and magnetic fields (Evans 1999, Krumholz et al. 2014).

The inclusion of 'feedback' in simulations of star formation has a profound effect on the accretion, multiplicity, and mass of protostars, with implications for the shape of the initial mass function and formation of star clusters (Offner et al. 2014, Bate et al. 2014, Krumholz 2014). Feedback processes in low- and high-mass star forming regions are associated with high temperatures ($\gtrsim$ 100K) and are thus not traced by the emission from cold dust. Instead, the high-temperature gas is being cooled in far-infrared molecular transitions (Goldsmith & Langer 1978). Quantifying this line emission is therefore crucial to identify additional physical processes in the surroundings of young stars and ultimately estimate their impact on the molecular clouds (Bate et al. 2014, Sales et al. 2014) and galaxy formation (Vogelsberger et al. 2014).

Validation of those simulations requires that the basic physical phenomenon are quantitiatively understood: *What are the physical conditions of the gas (temperature, density) in low- and high-mass star forming regions? What are the dominant physical processes responsible for the gas heating (shocks, ultraviolet radiation)? How does the evolution proceed to the point where the envelope is fully dispersed and the stars become visible in the optical light? How does the process differ for stars of different mass?*

Temperatures and densities of the physical regimes involved in the star formation process are best probed by far-infrared lines of in particular CO and H_2O whose excitation depends on the local physical conditions. The combination of excitation studies and spectroscopy at high enough angular resolution presents the ideal tools to quantify which physical mechanisms are responsible for the gas heating.

This thesis presents spectral observations of low- and high-mass star forming regions at different evolutionary stages using the PACS instrument (Poglitsch et al. 2010) on board the 3.5 m *Herschel Space Observatory* (Pilbratt et al. 2010a) that allow us to quantify the far-infrared emission at unprecedented detail and shed new light on the feedback from deeply embedded protostars.

Table 1.1 – Physical characteristics of interstellar and circumstellar clouds

Name	Density (cm^{-3})	Temperature (K)	Extinction (mag)	Examples
Diffuse cloud	10^2	30-100	1	ζ Oph
Translucent cloud	10^3	15-50	1-5	HD 154368
Dense PDR	$10^4 - 10^5$	50-500	< 10	Orion Bar
Molecular cloud	10^2	10-20	> 10	Perseus cloud
Dense core	$\gtrsim 10^5$	8-15	10-100	L1544
Protostellar envelope				
low-mass	$10^4 - 10^6$	8-100	10-100	L 1527
high-mass	10^4-10^7	20-100	50-500	AFGL 2591

Notes. The table presents typical physical parameters and is based on Table 2 from van Dishoeck et al. (2013), but with envelope parameters split into low- and high-mass protostars based on van der Tak et al. (2000, 2013), Jørgensen et al. (2002), Kristensen et al. (2012). The examples for diffuse and translucent clouds are the objects along their line-of-sight.

1.1 Interstellar medium and sites of star formation

Galaxies are mostly empty volumes with only a small fraction of space filled by stars and their planetary systems (e.g. $\sim 3\times10^{-10}$ of space in Milky Way, Tielens 2010). Everything in between stars is referred to as interstellar medium (ISM). The main visual manifestations of the otherwise hidden ISM are nebulosities seen around some young stars (e.g. reflection nebulae in the Pleiades) and some evolved stars (e.g. planetary nebulae and supernova remnants). In general, the diffuse and cold ISM is best revealed by absorption lines. The youngest stars are formed in the densest condensations of the ISM, which are opaque to visual light and seemingly devoid of stars.

Physical conditions in various clouds in the cold phase of the ISM are summarized in Table 1.1. The regions range from low-density diffuse and translucent clouds to dense photodissociation regions (PDRs, Tielens & Hollenbach 1985), illuminated by far-ultraviolet photons from nearby OB stars (FUV; 6 – 13.6 eV). Molecular clouds are regions with densities comparable to some PDRs but higher visual extinction (A_V) and thus more efficient UV shielding. The high density, low temperature regions of molecular clouds are dense cores, the sites of star formation. When the collapse begins, most of the material will accumulate in the envelope, the mass reservoir for the forming star(s).

Most stars in our Galaxy form in the Giant Molecular Clouds, which have masses as high as $\sim 10^{6.5}$ $M_\odot$ (Rosolowsky 2005) and projected areas of a few 10^3 pc^2 (Solomon et al. 1987). The most local star formation, however, occurs in smaller clouds, like the Perseus molecular cloud with $M \sim 7 \cdot 10^3$ $M_\odot$ and total area of 73 pc^2 (Evans et al. 2014). Even smaller are the Bok globules, clouds with masses of 1-100 $M_\odot$. The most striking common characteristics of those seemingly different environments are the uniform distribution of stellar masses that they form ('initial mass function') and the small number of stars formed given the available reservoir of gas and dust (Bastian et al. 2010). The star formation efficiency, defined as a fraction of stellar mass to the total mass in the cloud and

stars, is only about 3-6% in the nearby molecular clouds (Padoan et al. 2014).

Simulations of molecular clouds reproduce the shape of initial mass function and low star formation efficiencies when feedback from protostars is included (Krumholz et al. 2014). For example, feedback from outflows driven by low-mass protostars adds turbulence to the cloud, while UV heating suppresses the fragmentation and slows down the infall of material onto the protostar (Offner et al. 2014, Bate et al. 2014, Krumholz 2014). On the other hand, recent results from extinction mapping and from the 'Herschel Gould Belt Survey' show large similarities between the stellar and pre-stellar core mass functions (within a factor of 3), suggesting that no additional physical processes are required, i.e. the role of feedback is not dominant (Alves et al. 2007, André et al. 2010, 2014). A better understanding of physics and chemistry in the immediate surroundings of protostars is therefore needed to resolve these discrepant results and link the star formation on local and global scales.

1.2 Evolution before the main sequence

1.2.1 From dense cores to stars and planets

Figure 1.1 illustrates the key phases of low-mass star formation. The star formation begins once enough cold material condenses in the dense core, leading to its collapse under self-gravity (i.e. the criteria for Jeans instability are satisfied, Jeans 1928). Larson (1969) first described the main stages of this collapse, in particular the *Initial isothermal phase* when, due to pressure gradients, the small region with high density quickly develops in the core center; the *Formation of the opaque core*, where adiabatic collapse leads to the formation of the first hydrostatic core (radius of ∼5 AU and mass of ∼5 Jupiter masses) and the *Formation of the second (stellar) core,* triggered by dissociation of H_2.

The formation of the stellar core marks the beginning of the Class 0 phase. During this phase, referred to by Larson as the *main accretion phase,* material from the dense envelope is accreted to the star-disk system, quickly increasing the mass of the central protostar. The infall / accretion of material on the rotating protostar in the presence of magnetic fields leads to the launching of bipolar jets in the direction perpendicular to the disk, see recent review by Frank et al. (2014). The collimated jets carve out cavities in the surrounding envelope, exposing the material to the stellar winds and UV photons. As a result, wider-angle bipolar outflows are formed, with shocks and entrainment occurring along the cavity walls. Such a low-mass protostar with its envelope and outflows is altogether referred to as a *young stellar object* (YSO).

The subsequent evolution of a protostar is determined by accretion onto the disk/star system and simultaneous dispersal of the envelope by the outflows (Class I). The UV radiation from the growing central star penetrates deeper into the envelope, while the jets carry less material as the accretion rate decreases and eventually stops. Once the envelope disappears (Class II), a central pre-main sequence star surrounded by a circumstellar disk becomes visible. The gas from the disk is trapped in the giant planets or dispersed by the strong stellar wind and radiation. Subsequently, the grains in the disk coagulate to larger

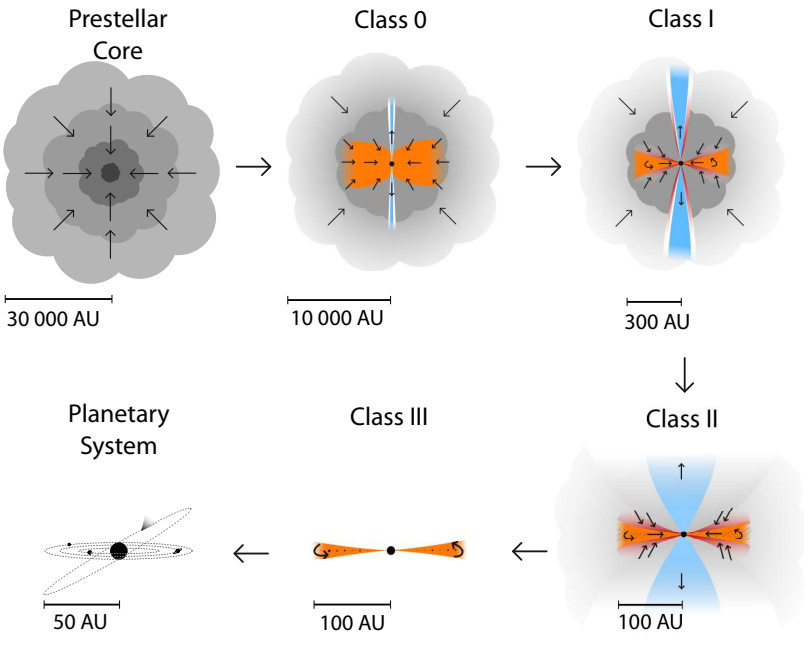

Figure 1.1 – Evolution of a collapsing dense core to a Sun-like star with a planetary system. The physical scales are indicated for each evolutionary stage. Adapted from Persson (2013).

particles, leading to the planetesimal and planet formation (Class III).

The evolution of protostars is therefore driven by the relative amount of mass in the envelope ($M_{\rm env}$), central protostar ($M_\star$), and the disk ($M_{\rm disk}$). Physical classification based on the masses distinguishes four main Stages ((0-III), Robitaille et al. 2006, 2007) that ideally should correspond to more phenomenological Classes used in this thesis and in Figure 1.1. In the Stage 0 sources the envelope mass is much larger than that of the central protostar, $M_{\rm env} \gg M_\star$. In Stage I, the envelope mass becomes less than the mass of the protostar, $M_\star > M_{\rm env}$. In Stage II, the disk mass is larger than that of the envelope, $M_{\rm disk} > M_{\rm env}$. Unfortunately, determining masses directly from observations is difficult (Crapsi et al. 2008) and therefore alternative methods of classification have been developed.

1.2.2 Observational classification of young stellar objects

The evolution of young stellar objects is revealed by the shapes of their spectral energy distributions (SEDs). The SEDs of Class 0 sources are dominated by emission from cold dust, whereas the contribution from the star-disk system increases gradually in more evolved Class I/II sources (Figure 1.2 and Chapter 2). Several methods are used to quan-

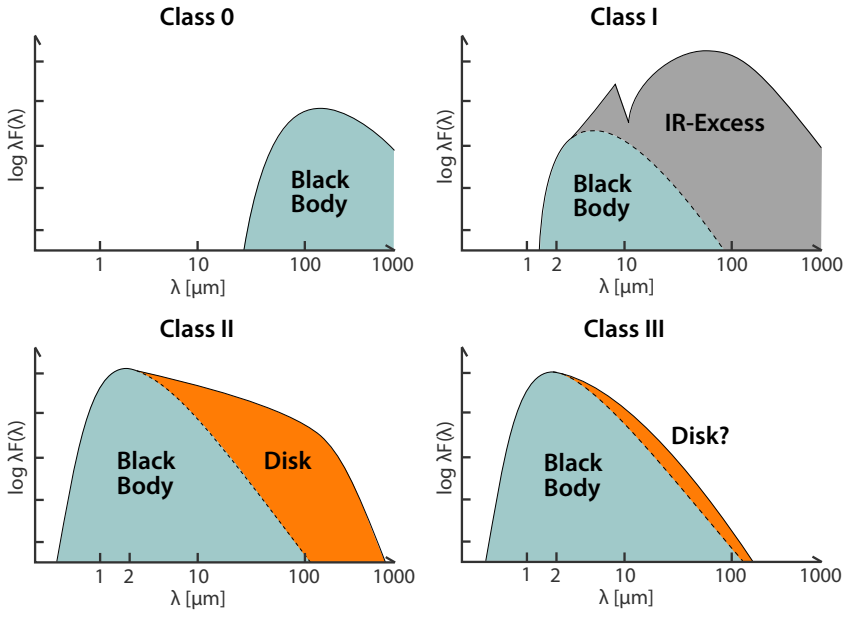

Figure 1.2 – Spectral energy distributions of low-mass young stellar objects. Class 0 sources are characterized by a single black-body spectrum from the cold envelope peaking at ~100 μm (no emission in near-IR). Class I sources have lower extinction and thus a protostellar black body spectrum slowly appears in the near-IR with a large IR excess ('rising SED') at longer wavelengths due to the remaining envelope and growing disk. Class II sources have flat or falling SEDs consisting of a pre-main sequence (T Tauri) stellar black-body and disk emission at mid- to far-IR. Class III sources show a stellar spectrum (more luminous than the main-sequence stars) with a possible weak contribution from the remaining disk. Figure by M. Persson.

tify the SEDs and construct the age sequences of protostars (for detailed discussion, see Evans et al. 2009).

Their main shortcoming is the uncertainty in the outflow/disk geometry, which can severely alter the shape of the SED. For example, when the disk is viewed face-on, mid-IR emission is easily detected by looking down the outflow cone, mimicking the more evolved sources. On the other hand, the edge-on disks hide the protostellar contribution, and the SED is thus dominated by the cold envelope making the source appear less evolved.

Table 1.2 summarizes how Class 0 and I sources are defined using different classification methods. The method based on the spectral index, α, introduced by Lada & Wilking (1984) and extended by Greene et al. (1994), uses the SED between 2 and 20 μm and is not suitable for classification of Class 0 sources. Bolometric temperature, $T_{\rm bol}$, defined as the temperature of a blackbody with the same flux-weighted mean frequency as the actual SED, is calculated over the entire spectrum and divides sources into Class 0 and I at 70

Table 1.2 – Classification of Class 0/I protostars

Method	Class 0	Class I	Reference
α^a	–	0.3	Lada & Wilking (1984), Greene et al. (1994)
$T_{\rm bol}$	< 70	$70 < T_{\rm bol} < 650$	Myers & Ladd (1993), Chen et al. (1995)
$L_{\rm submm}/L_{\rm bol}$	> 200	< 200	André et al. (1993),Young & Evans (2005)
$L_{\rm bol}^{0.6}/M_{\rm env}$	$< 2^b$	2^b	Bontemps et al. (1996)
$L_{\rm FIRL}/L_{\rm bol}{}^c$	$\sim 10^{-2}$	$\sim 10^{-3}$	Giannini et al. (2001), Nisini et al. (2002b)

Notes. $^{(a)}$ Spectral index, $\alpha = d\log(\lambda S(\lambda))/d\log\lambda$, calculated using SED between 2 and 20 μm (λ is the wavelength and $S(\lambda)$ is the flux density at that wavelength). Class 0 sources with SEDs resembling a blackbody spectrum at $T \sim 15 - 30$ K could not be classified in this scheme due to non-detections in mid-IR wavelengths. $^{(b)}$ For a protostar with bolometric luminosity $L_{\rm bol} = 1\ {\rm L}_\odot$. $^{(c)}$ Far-infrared line cooling, $L_{\rm FIRL}$, is the sum of $L_{\rm O\,I} + L_{\rm CO} + L_{\rm H_2O} + L_{\rm OH}$.

K (Myers & Ladd 1993). According to models of collapsing cores by Young & Evans (2005), the ratio of source luminosity longwards of 350 μm and its bolometric luminosity is a good indicator of the ratio of mass in the star and the envelope (see also, André et al. 1993); the $L_{\rm bol}/L_{\rm submm}$ ~200 marks the transition from Class 0 to I. A tight correlation between envelope mass and bolometric luminosity in Class 0/I protostars led Bontemps et al. (1996) to describe the evolutionary stage using the $L_{\rm bol}^{0.6}/M_{\rm env}$ ratio.

Far-IR lines are not sensitive to extinction and are often optically thin (e.g. highly-excited CO lines); as such, they provide an alternative to continuum slopes for determining the evolutionary stage. Giannini et al. (2001) introduced a parameter $L_{\rm FIRL}$, the total line luminosity of species emitting in the far-IR, which decreases for more evolved sources. The underlying assumption was that the dominant excitation mechanism of far-IR emission (most likely outflow shocks) decreases in strength with evolution. If that is indeed the case, $L_{\rm FIRL}$ could serve as the most accurate evolutionary tracer of protostellar evolution.

1.3 Heating and cooling in deeply-embedded protostars

1.3.1 Processes leading to gas heating

Figure 1.3 illustrates the main physical components of low-mass YSOs that can give rise to far-IR line emission. Possible components include (i) the inner part of the envelope heated by the accretion luminosity (hot core); (ii) the entrained outflow gas; (iii) UV-heated gas along the cavity walls; (iv) shocks along the outflow cavity walls where the wind from the young star directly hits the envelope; (v) bow shocks at the tip of the jet where it impacts the surrounding cloud; (vi) internal working surfaces within the jet; and (vii) a disk embedded in the envelope. The contribution of these components to the far-IR emission from deeply-embedded YSOs is evaluated and discussed below.

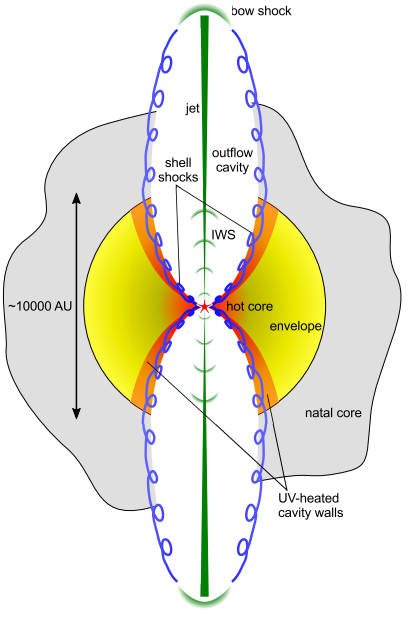

Figure 1.3 – Cartoon of a low-mass young stellar object with various physical components and their nomenclature indicated. IWS stands for internal working surfaces. The spatial scales correspond to low-mass protostars and do not resolve the ~100 AU disk surrounding the protostar. Figure by R. Visser, adapted from van Dishoeck et al. (2011).

1.3.1.1 Envelope heating by protostellar luminosity

The main source of protostellar luminosity during the Class 0/I phase is the *accretion luminosity* produced from the gravitational energy of the infalling gas from the dense collapsing envelope, through the disk, and onto the star in extremely hot ($>10^5$ K) accretion shocks. This luminosity heats mostly the inner parts of the envelope, since the large amount of dust quickly absorbs most of the protostellar radiation and re-radiates it in the form of far-IR continuum. The gas is then heated through gas-dust collisions. However, a fraction of the envelope cooling is also predicted to occur via atoms and molecules (Ceccarelli et al. 1996, Doty & Neufeld 1997, for early models of line emission from low- and high-mass envelopes, respectively).

Far-IR H_2O emission was initially interpreted as arising purely from the collapsing envelope in Class 0/I sources (Ceccarelli et al. 1999) based on the single beam observations ($\sim$ 80″) with the Long-Wavelength Spectrometer on board the *Infrared Space Observatory* (ISO) (Kessler et al. 1996, Clegg et al. 1996). However, small maps with the same instrument revealed that the emission is extended and more likely originates in the outflow (Nisini et al. 1999). Recently, Visser et al. (2012) concluded that the envelope cooling accounts for less than 1% of the total H_2O emission and only a few percent of CO

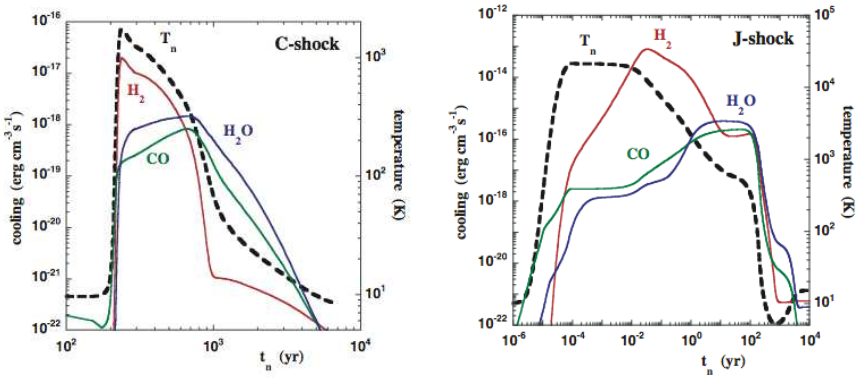

Figure 1.4 – Rates of molecular cooling as a function of flow time of neutrals in $C-$ (left) and $J-$type (right) shocks with v=20 km s^{-1} and pre-shock density of the ambient medium $n = 10^5$ cm^{-3}. The temperature structure through the shock is shown on the right vertical axis. Adapted from Flower & Pineau des Forêts (2010).

emission observed towards low-mass protostars with *Herschel*/PACS.

1.3.1.2 Shocks in outflow cavities and jets

Large-scale shocks are produced by the bipolar jets and protostellar winds impacting the envelope along the cavity walls. Theoretically, shocks are divided into two main types, the 'continuous' (*C*-type) and 'jump' (*J*-type) shocks, based on a combination of magnetic field strength, shock velocity, density, and level of ionization (Draine 1980, Draine et al. 1983, Hollenbach et al. 1989, Hollenbach 1997).

In $C-$type shocks, which occur in regions with strong magnetic fields and low ionization fractions, the weak coupling between the ions and neutrals results in a continuous change in the gas parameters (for an example of temperature profile, see Figure 1.4). Peak temperatures of a few 10^3 K allow the molecules to survive the passage of the shock, which is therefore referred to as non-dissociative.

In $J-$type shocks, physical conditions change in a discontinuous way, leading to higher peak temperatures than in *C* shocks of the same speed and for a given density (Figure 1.4). Depending on the shock velocity, *J* shocks are either non-dissociative (velocities below about $\sim$ 30 km s^{-1}, peak temperatures of about a few 10^4 K) or dissociative (peak temperatures even exceeding 10^5 K), but the molecules efficiently reform in the dense post-shock gas (Figure 1.4).

Cooling of post-shock gas by H_2 is dominant in the outflow shocks, but negligible for lower$-T$ gas due to a lack of low-lying rotational states and the large level spacing in H_2 (Goldsmith & Langer 1978). But even in regions with sufficiently high temperatures, mid-IR H_2 emission is strongly affected by extinction in the dense envelopes of young protostars (Davis et al. 2008, Maret et al. 2009). The far-IR rotational transitions of H_2O

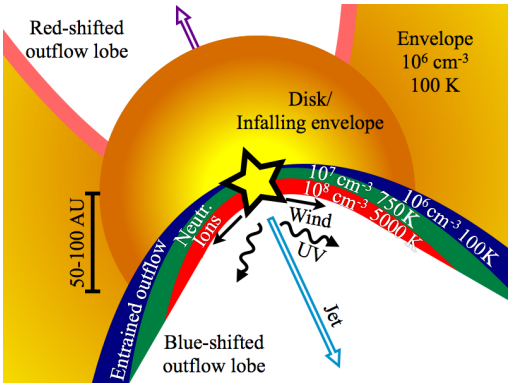

Figure 1.5 – Cartoon illustrating the inner regions of protostellar envelope where UV radiation from the protostar can dissociate the shocked gas and produce high−J CO emission ($J_{up} \gtrsim 24$). Adopted from Kristensen et al. (2013).

and CO are thus a better diagnostic of the shock type, shock velocity, and the pre-shock density of the medium (Hollenbach et al. 1989, Kaufman & Neufeld 1996, Flower & Pineau des Forêts 2010, 2012).

The characteristics of the first complete far-IR spectra of low-mass Class 0/I protostars obtained with ISO /LWS indicated an origin in the two distinct shocks (Giannini et al. 2001, Nisini et al. 2002b). The molecular emission was attributed to the slow, C−type shock in the cavity walls and the bright [O I] emission arising from the J−type shock in the jet and / or bow-shock. A fraction of the [O I] emission was also attributed to the UV heating from the protostar. The [O I] contribution to the total cooling was higher for the more evolved sources.

This general picture finds support in the recent observations with *Herschel*, even though the details of the shock characteristics are still strongly debated. The [O I] emission is generally explained by J−type shocks (van Kempen et al. 2010b, Benedettini et al. 2012, Dionatos et al. 2013, Lee et al. 2013, Santangelo et al. 2013), but a convincing detection of the high velocity component is seen only towards low-mass source HH46 (van Kempen et al. 2010b). The molecular emission is attributed to slow ($v \sim 15 - 40$ km s^{-1}), non-dissociative $C-$ or J−type shocks, depending on the assumptions on the (spatially unresolved) size of the emitting region and the exact species (CO, H_2O, OH, H_2) that are treated together. An alternative explanation for the very high−J CO emission is dissociative shocks due to strong UV irradiation proposed by Kristensen et al. (2013), see Figure 1.5.

1.3.1.3 Ultraviolet heating and gas entrainment in the outflow cavity walls

The first observations of ^{13}CO $J = 6 - 5$ in low-mass protostars showed unexpectedly intense, extended line emission that could not be accounted for by the models of collapsing

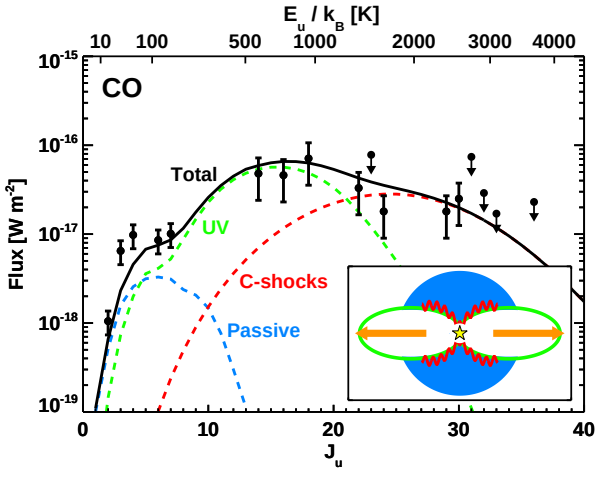

Figure 1.6 – CO fluxes observed with *Herschel* / PACS and APEX telescope (J_u<10) with model predictions from a passively heated envelope (blue), a UV-heated cavity (green), and small-scale shocks in the cavity walls (red). The black line is the sum of the three. A cartoon of the different components is shown in the inset. Adopted from van Kempen et al. (2010b).

envelopes (Spaans et al. 1995, Hogerheijde et al. 1997). Spaans et al. (1995) explained this puzzling excess emission with additional heating of cavity walls by the ultraviolet photons from the ∼10,000 K boundary layer where the accretion stream hits the star, scattered in the low-density outflow cavities. van Kempen et al. (2009a) adopted this model to describe the extended CO $J = 6 - 5$ emission in the HH46, but with additional UV photons created in the dissociative $J-$type shocks originating in the internal working surfaces in the jet and / or in the bow-shock at the tip of the jet (Neufeld & Dalgarno 1989).

The UV heating was subsequently invoked to explain the bulk of CO $J_{\rm up} \sim 10 - 20$ emission detected with *Herschel* / PACS (van Kempen et al. 2010b, Visser et al. 2012). In models of HH 46 (Figure 1.6), 45% of the total CO emission is excited by UV heating, 48% is excited in small scale $C-$type shocks, and 7% is excited in the passively heated envelope (Visser et al. 2012). Modeling of two additional sources in Visser et al. (2012) showed that the contribution of the UV heating to the total line cooling increases as the protostar evolves, from ∼20% in the young Class 0 protostar up to ∼80% in Class I/II protostar.

Yıldız et al. (2012) used the velocity-resolved profiles of CO isotopologues to directly measure the amount of gas traced by CO 2 – 1 to 10 – 9 lines in the envelope, outflow, and UV heated component (see Figure 1.7). First, the density and temperature gradients in the envelope were modeled using the continuum maps. The narrow $C^{18}O$ line profiles produced in the envelope emission were used to constrain the CO abundance profile in the envelope (following the approach in Jørgensen et al. 2002). Subsequently, the resulting envelope structure was used to calculate the fraction of ^{13}CO emission that arises from

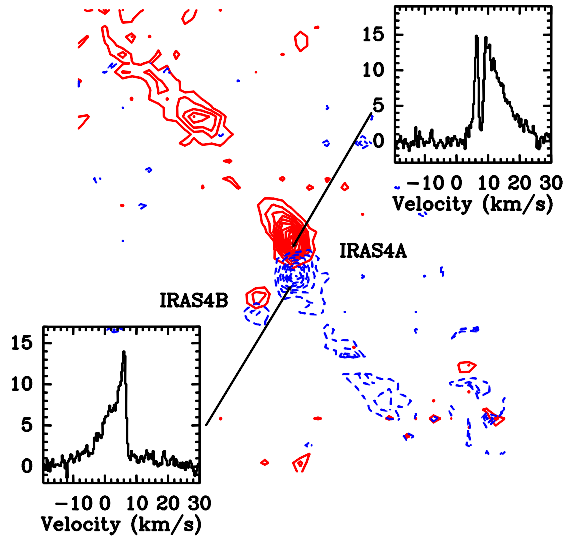

Figure 1.7 – ^{12}CO 6-5 line profiles at the blue and red outflow positions of NGC 1333 IRAS 4A. The integrated emission in the blue (-20 to 2.7 km s^{-1}) and red (10.5 to 30 km s^{-1}) velocity ranges with respect to the source velocity is shown as contours. Figure by U. A. Yıldız, based on Yıldız et al. (2012).

the envelope. The excess emission from the observations was proposed to arise in the UV-heated component (following van Kempen et al. 2009a,b), since the narrow shape of ^{13}CO line profiles and the low abundances of ^{13}CO with respect to the CO made the outflow origin unlikely. The emission in the broad component in the ^{12}CO line was interpreted as arising in the entrained outflow gas with a kinetic temperature of $\sim$ 100 K. The amount of gas mass in the UV-heated and the outflow components was found to be comparable.

1.3.2 Main cooling channels

Any single dust grain located in Class 0/I envelopes absorbs ultraviolet photons from the central protostar, heats up, and then cools by emitting radiation at far-infrared wavelengths. This cooling channel is the dominant source of far-IR continuum radiation. The resulting far-IR continuum is thus an excellent tracer of envelope properties (size, density, temperature) that can be derived from simple modified blackbody fitting (e.g. Goicoechea et al. 2012) or more complicated radiative transfer models (e.g. Young & Evans 2005, Kristensen et al. 2012). On the other hand, the dust emission does not trace the warm gas of young stellar objects that is heated directly by shocks or the photoelectric effect in other physical components and can only be studied using lines.

Goldsmith & Langer (1978) made the first predictions of molecular and atomic line emission from dense interstellar clouds. Although the knowledge of abundances of vari-

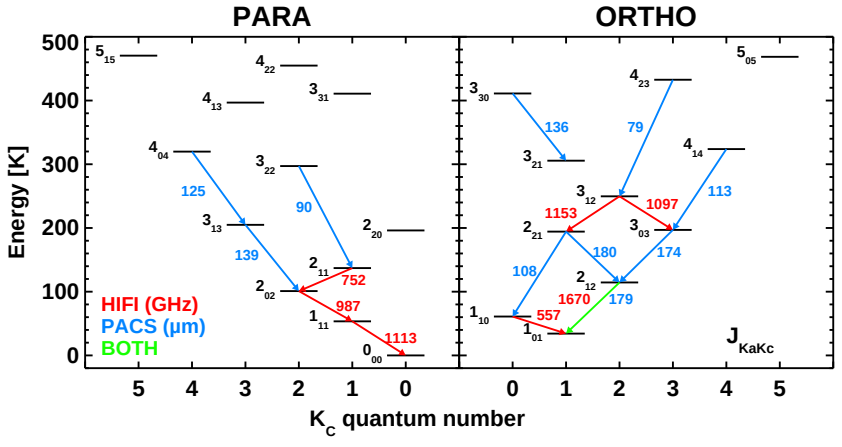

Figure 1.8 – Energy levels of ortho- and para-H_2O with some important transitions observed in the WISH program with *Herschel* / PACS (in μm) and *Herschel* / HIFI (in GHz) indicated (adopted from van Dishoeck et al. 2011). In fact, as many as $\sim$ 65 H_2O lines were detected with PACS in NGC 1333 IRAS 4B (Herczeg et al. 2012).

ous species was scarce, the models based on the energy level structure, Einstein coefficient for spontaneous emission (A), and the collision rate coefficients were mostly correct. For densities $\gtrsim 10^4$ cm^{-3} and $T \sim 10$ K, a large number of species including H_2O, hydrides (e.g. OH), molecular ions (emitting in the sub-millimeter regime), and diatomic molecules (e.g. CO) dominated the total line cooling. Neufeld & Kaufman (1993) extended these predictions to warmer gas ($T \gtrsim 100$) of similar densities, focusing on H_2, H_2O, and CO, and suggested that H_2O may be even the dominant coolant in such gas if its predicted high abundances are correct. The other reasons for the dominant role of H_2O, CO, and a possible importance of OH, in gas cooling are discussed below.

1.3.2.1 H_2O

The routes of H_2O formation include ion-molecule reactions at $T \sim 10$ K, very efficient high temperature neutral-neutral reactions in shocked gas ($T \gtrsim 230$ K), and formation on the grains (ice abundances as high as 10^{-4}) followed by evaporation into the gas phase at $T \sim 100$ K (van Dishoeck et al. 2011, 2013). In dense and relatively warm environments of young protostars, the abundances of H_2O are expected to be high.

H_2O is an asymmetric rotor molecule with a large number of energy levels contributing to the total cooling (Figure 1.8). Rotational levels are characterized by rotational quantum number J and two additional quantum numbers K_A and K_C, which relate to the projection of the angular momentum on the axes of symmetry. The nuclear spins of the two hydrogen atoms can be either parallel or anti-parallel, resulting in a grouping of the rotational levels into ortho ($K_A + K_C$ = odd) and para ($K_A + K_C$ = even) ladders.

The large dipole moment (μ_D=1.85 D) of H_2O and the high frequencies (ν) of the transitions result in relatively large spontaneous radiative rates compared to other molecules, proportional to $\mu_D^2\nu^3$ (Einstein A coefficients). Therefore, H_2O is de-excited by line emission (radiation) and not by collisions in protostellar envelopes, where densities are a few orders of magnitude lower than the critical density needed for thermalization. That implies that the level population typically cannot be described by a Boltzmann distribution at the gas kinetic temperature; the rotational temperature calculated based on H_2O lines is therefore set by a combination of the temperature and density.

Giannini et al. (2001) first quantified the role of H_2O in the total gas cooling in Class 0 protostars using the complete far-infrared spectra obtained with ISO/LWS. H_2O, CO, and [O I] were found to contribute each $\sim$ 30% of the total gas cooling, with the remaining emission originating in OH. Nisini et al. (2002b) extended this study to Class I sources and demonstrated a decrease in molecular cooling as a protostar evolves.

1.3.2.2 CO

CO is the second most abundant molecule in the ISM after H_2 ($CO/H_2 = 10^{-4}$) with level energies scaling as $\propto J(J+1)$ (Figure 1.9). Due to the relatively high mass of the molecule the levels are closely spaced, with the few lowest$-J$ transitions lying at sub-/mm wavelengths and $J \gtrsim 10$ in the far-IR. In contrast to H_2O, CO has a very small dipole moment (μ_D=0.1 D) and its low$-J$ transitions are easily collisionally excited even at low densities, providing a better diagnostic of gas kinetic temperature.

CO lines with upper levels as high as $J_{up} = 49$ and 36 CO lines in total have been detected with *Herschel*/PACS towards low-mass young stellar objects (Herczeg et al. 2012, Goicoechea et al. 2012, Green et al. 2013, Manoj et al. 2013). Such a large number of transitions contribute a significant fraction of the total line cooling, but can also prove useful in determining the physical conditions of gas (its temperature and density) in young protostars. In fact, many protostars observed with PACS show CO emission at two (rotational) temperatures, $\sim$ 350 K and $\gtrsim$ 700 K, suggesting that the origin is in two distinct physical components (van Kempen et al. 2010b, Visser et al. 2012). Alternatively, the origin is in a single low-density, hot component (Neufeld 2012, Manoj et al. 2013). In either case, the physical origin(s) is not yet fully understood.

1.3.2.3 OH

OH is a free radical i.e., it has one unpaired electron, and thus its energy levels are divided into two ladders corresponding to opposite orientations of the unpaired electron spin with respect to Λ, the projection of angular momentum on the molecular axis (Figure 1.9). The levels are further split into two configurations, depending on whether the symmetry axis of the unpaired electron orbital motion is coincident or orthogonal to the internuclear axis (Λ-doubling). The interaction between the spins of the unpaired electron and the hydrogen nucleus results in magnetic hyperfine splitting (Tennyson 2005).

Although the OH abundances are not as high as those of CO, the cooling in OH can be important in regions where the high temperature route of H_2O formation is at play (at

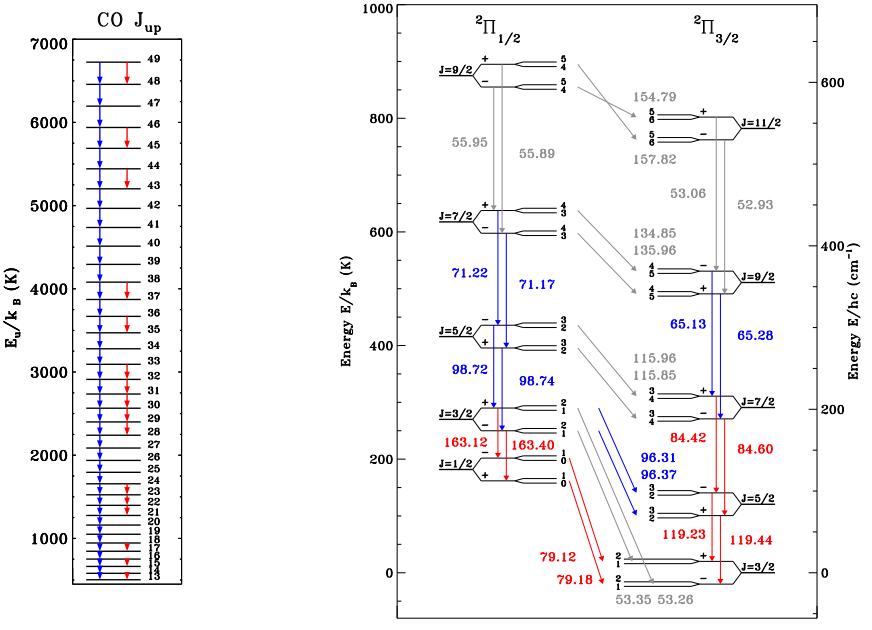

Figure 1.9 – Energy levels of CO (right) and OH (left) observed with *Herschel* / PACS. Blue arrows indicate transitions detected towards low-mass protostars in the full-spectrum mode, while red arrows indicate the lines targeted and detected towards most sources in the WISH program. The OH diagram is adopted from Wampfler et al. (2013).

$T \gtrsim$230 K). The backward reaction leading to the H_2O destruction and OH formation requires hydrogen in the atomic form and therefore depends on the local UV field or presence of dissociative shocks (Wampfler et al. 2013). These conditions can occur in $J-$type shocks along the jet or in a bow shock or in UV-irradiated cavity shocks in low-mass young stellar objects and thus explain the relatively large OH cooling, ∼3% in Class 0 and ∼ 20% in Class I sources (this thesis, Karska et al. 2013).

1.4 *Herschel* / PACS

Herschel was a 3.5 m space telescope operating from mid-2009 to mid-2013 at the L2 point located 1.5 10^9 m 'behind' the Earth as viewed from the Sun (Pilbratt et al. 2010a). The telescope was equipped with three complementary instruments designed for observations at the far-infrared and submillimeter wavelengths:

- HIFI – the Heterodyne Instrument for the Far-Infrared (de Graauw et al. 2010) –

a single pixel heterodyne spectrometer observing at 480-1910 GHz (157-625 μm) with very high spectral resolving power, R= $\lambda/\Delta\lambda \gtrsim 10^6$ (dv $\sim$ 0.1 km s^{-1}) and diffraction limited beam of ~11-45".

- PACS – the Photodetector Array Camera and Spectrometer (Poglitsch et al. 2010) – consists of two subinstruments: an imaging photometer and an integral-field spectrometer, both sensitive to emission at 50−210 μm with blue and red bands observed simultaneously. The photometer consisted of two bolometer arrays with 16×32 and 32×64 pixels covering a field of view 1.75'×3.5' in the 60-85 μm / 85-125 μm and 125-210 μm bands. The spectrometer consisted of a 5×5 array of spaxels, each corresponding to 9.4"×9.4" on the sky, and a total field of view of 47"×47". The spectral resolving power is R~ 1000 – 5500 (dv ~ 60 – 320 km s^{-1}) depending on the grating order.

- SPIRE – the Spectral and Photometric Imaging Receiver (Griffin et al. 2010) – an imaging photometer and an imaging Fourier transform spectrometer observing at 194-672 μm with spectral resolution R~ 40 – 1000 at 250 μm.

A more detailed description of the PACS spectrometer and its comparison to the Long Wavelength Spectrometer on ISO are presented in the following sections.

1.4.1 PACS spectrometer

The key scientific goal of the PACS spectrometer was to provide medium resolution observations (R~ 1500) of weak spectral lines on top of a much stronger far-infrared continuum, particularly of extragalactic sources (Poglitsch et al. 2010). In order to achieve the required sensitivity, but also the sufficient baseline coverage and high tolerance to pointing errors without compromising spatial resolution, the integral-field unit (IFU) design was selected.

In the PACS IFU spectrometer, the two dimensional image from the 5×5 array is transformed by the image slicer into a one dimensional entrance slit for the grating spectrometer, as illustrated in Figure 1.10. The spectrometer consists of two Ge:Ga photoconductors arrays (for blue and red bands) with 16 spectral elements and 25 spatial pixels (*spaxels*), that determine the spectral and spatial resolution of the instrument.

The grating is operated in the 1st, 2nd, and 3rd orders to cover the full wavelength range, with special order sorting filters suppressing contributions by other orders. The respective wavelengths are 102-210 μm (1st order), 71-105 μm (2nd), and 51-73 μm (3rd), but the order overlap regions and spectrum > 190 μm is not instantly usable (see Appendix A in Herczeg et al. 2012).

The resolving power increases non-linearly with wavelength, with R~1000-2000 in the 1st order, R~1500-3000 in the 2nd order, and R~2500-5500 in the 3rd order. The corresponding velocity resolution ranges from ~90 km s^{-1} in the 3rd order observation of the [O I] line at 63 μm to ~300 km s^{-1} in the CO 24-23 line at 108 μm. As a result, typically the lines are spectrally unresolved (Gaussian shape), with only a few sources showing high-velocity wings in the [O I] profiles. Spectral coverage (covered by 16 pixels)

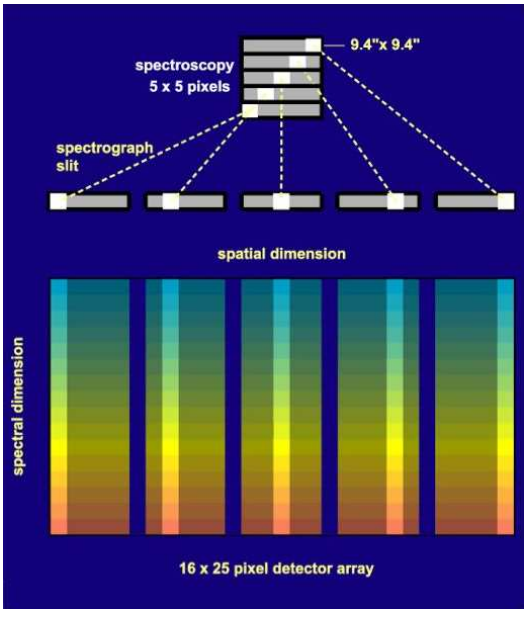

Figure 1.10 – Integral-field spectroscopy with PACS. The 5×5 array of spaxels is re-arranged by the image slicer along the entrance slit of the grating spectrograph to observe simultaneously all 25 spectra. Adopted from the PACS Observer's Manual (http://herschel.esac.esa.int/Docs/PACS/html/pacs_om.html).

is about 1400 km s^{-1} at 63 μm and 3000 at 108 μm, with typically 1-2 pixels per full width half maximum (FWHM), respectively.

The telescope point spread function (PSF) is asymmetric, with the size increasing with wavelength and not diffraction limited below ~130 μm. As a consequence of the fixed size of the spaxels, the fraction of the PSF viewed by the spaxels differs depending on the wavelength. At 63 μm, the central spaxel views 70% of a perfect point-source emission, while at 186 μm (CO 14-13) only 42 % is captured. It is thus important to account for the flux outside the central spaxel, in particular when comparing line fluxes at different wavelengths.

The two main observing schemes on PACS were the line spectroscopy and the range spectroscopy modes. The line spectroscopy mode allows observations of small spectral regions ($\Delta\lambda$ ~0.5-2 μm) around selected lines and is particularly well suited for deep integrations. The range spectroscopy mode provides the full spectrum from ~ 50 to 210 μm but the spectral sampling within a resolution element is about 3-4 times coarser than in the line spectroscopy mode.

For both schemes, the chopping / nodding or the wavelength switching techniques were employed to subtract the far-IR background emission. In the chop/nod mode, spectroscopy of the region at a distance up to 6′ from the source was used to correct for

emission unrelated to the source. In cases where the contamination was still high at those distances, the signal is modulated by moving the line over about half of the FWHM and the differential line profile is measured.

1.4.2 Comparisons to ISO / LWS

The ISO/LWS was the only instrument before PACS that offered the access to the complete far-IR window, with a spectral range of 45-197 μm (Kessler et al. 1996, Clegg et al. 1996). The telescope was operational in 1995-1997.

ISO had a relatively small diameter of 0.6 m and thus the LWS beam was $\sim$ 80″, nearly an order of magnitude larger than in case of *Herschel* / PACS. As a consequence, the spatial information of the line and continuum emission was lacking. The emission in a single beam from protostars was often contaminated by nearby sources, their outflows, and the PDR emission from the cloud.

A factor of $\sim$ 6 increase in the telescope diameter and the IFU design of the PACS instrument provides an improved spatial resolution. As a consequence, the spatial extent of line emission coupled with the more accurate excitation analysis allows us to trace the origin of far-IR line and continuum emission. In particular, the [O I] and [C II] emission patterns demonstrate whether the emission is dominated by the large scale cloud PDR or a protostar.

The spectral resolving power of LWS was ~200, about a factor of 10 lower than PACS. The Fabry-Perot mode offered a higher spectral resolution, but the sensitivity was so low that only a few brightest sources could be observed. The higher spectral resolution and sensitivity of PACS with respect to LWS was therefore crucial to detect weak molecular lines, especially on top of the bright continuum. The CO lines up to $J_{\rm up}$ = 49 are detected in NGC1333 IRAS4B (20 more lines than with ISO!) and reveal two components on CO diagrams (Herczeg et al. 2012, Goicoechea et al. 2012, Manoj et al. 2013, Green et al. 2013). The detections of H_2O lines in Class I sources improve our understanding of the evolution of molecular cooling from Class 0/I protostars and allow us to model the physical conditions at which H_2O is produced (Herczeg et al. 2012).

1.4.3 WISH, DIGIT, and WILL programs

This thesis uses data from three large *Herschel* programs: WISH, DIGIT, and WILL. The ‘Water in Star forming regions with Herschel’ (WISH) is a guaranteed-time key program on *Herschel* with the primary goal to probe the physical and chemical processes in young stellar objects using H_2O and related species (van Dishoeck et al. 2011). The effects of evolution and environment on the molecular emission are studied by targeting sources at various evolutionary stages (from pre-stellar cores to Class II) and masses (low-, intermediate-, and high-mass protostars). The HIFI spectra of selected lines (Figure 1.8) are complemented with PACS maps in the line spectroscopy mode. Full PACS spectra are acquired for only 4 Class 0 sources. Fully-sampled maps of a few sources are obtained at the protostellar or outflow position (e.g. Nisini et al. 2010a), with most of the sources observed in a single pointing.

The 'Dust, Ice, and Gas in Time' (DIGIT) open time key program uses the full PACS 50-210 μm spectra of about 30 Class 0/I protostars to quantify the dust and gas evolution in the far-IR (Green et al. 2013). All the targeted sources have good quality mid-IR and sub-mm observations, which together with PACS spectra allow the determination of the full SED and the search for and analysis of solid-state features. The full inventory of far-IR gas lines provides a unique measurement of total far-infrared line cooling and is a useful guide for analysis of WISH / PACS data, where mostly selected lines were targeted.

The 'William Herschel Line Legacy' (WILL) survey obtained PACS and HIFI spectra toward an unbiased flux-limited sample of low-mass protostars newly discovered in the recent *Spitzer* and Herschel Gould Belt imaging surveys (e.g. Evans et al. 2009, André et al. 2010). Its main aim is to study the physics and chemistry of H_2O and related species in star-forming regions in a statistically significant way by doubling the sample of low-mass protostars observed in the WISH and DIGIT programs.

1.5 This thesis

The central theme of this thesis is the feedback from protostars onto their surroundings during the first 0.5 million years of protostellar life (Dunham et al. 2014). The feedback is elucidated by means of astrochemistry – the molecules and atoms are used as tracers of physical conditions of the emitting gas and the associated physical processes. Far-infrared spectroscopy from the *Herschel Space Observatory* (2009-2013) unravels the spatial scales and energetics of the protostellar feedback at unprecedented detail. Large *Herschel* surveys of protostars at various evolutionary stages and masses reveal global properties of young stellar objects and their evolution during the deeply-embedded stage that cannot be studied at visible wavelengths. The most important questions specifically addressed in this thesis are the following.

- What is the origin of far-infrared emission in the surroundings of young stellar objects? Can we quantify the feedback from protostars on envelope spatial scales using molecular lines of CO, H_2O, and OH, and atomic [O I]?
- What is the role of shocks and ultraviolet radiation in low-mass protostars and on which scales?
- What is the cooling budget of hot gas in deeply-embedded protostars? Which feedback processes determine the total line cooling?
- How do physical processes responsible for the gas heating change with evolution? How robust is the total gas cooling as an evolutionary tracer?
- What is the impact of protostellar mass on the properties of the far-infrared emission? Are the dominant excitation mechanisms of CO the same in low- and high-mass star forming regions?

These questions are addressed in the following chapters. The names of the projects on *Herschel* where the data come from are shown in brackets next to the chapter titles.

Chapter 2 – *Far-IR cooling lines in low-mass young stellar objects* [WISH]

A spectral survey of 18 low-mass protostars reveals rich molecular and atomic far-infrared emission. CO lines from J =14-13 to J = 49 – 48 and even highly-excited H_2O lines (for example, the H_2O 8_{18}–7_{07} line with the upper level energy above 1000 K) are detected. Boltzmann diagrams of CO show two temperature components, at ~350 K and ~700 K, whereas H_2O diagrams show a single component at ~150 K and a significant scatter due to subthermal excitation. A broad range of corresponding gas physical conditions is found using non-LTE radiative transfer calculations. Similar patterns of spatially-extended H_2O and CO emission and their strong flux correlations found in the survey indicate high-densities ($n_{\rm H} \gtrsim 10^6$ cm^{-3}) and moderately-high temperatures ($T_{\rm kin} \gtrsim 350$ K) of the exciting gas. Comparisons to shock models yield consistent results suggesting that *H_2O and CO originate most likely in non-dissociative shocks*. In contrast, at least a fraction of OH and [O I] emission originates in a different physical component, since no spatial or strong flux correlations are found between those species and CO or H_2O. Dissociative shocks at the point of direct impact of the wind on the dense envelope are the most likely excitation mechanism, since only a small fraction of [O I] emission is seen in the high-velocity wings tracing a hidden atomic jet. The total far-infrared gas cooling budget is dominated by H_2O and CO (up to 50%) with an increasing contribution of [O I] for more evolved sources (up to 30% of total cooling). The absolute value of the total gas cooling and its ratio with the source bolometric luminosity decrease with evolution from Class 0 to Class II sources and therefore are useful evolutionary tracers.

Chapter 3 – *Far-IR molecular lines from low- to high-mass star forming regions* [WISH]

A survey of 10 high-mass star forming regions extends the study of low-mass protostars from Chapter 2 to more massive objects. Rich far-infrared molecular spectra are detected at the central position of PACS maps. Many H_2O lines are detected in absorption against the bright continuum emission, in particular at shorter wavelengths, and do not contribute to the gas cooling. Instead, the total cooling is dominated by CO (typically ~75%) and [O I] (~20%) with a minor contribution of H_2O and OH (below ~1%). Even though CO transitions up to $J_{\rm up} \sim 29$ are detected, only one temperature component at $\sim$ 300 K is seen on the CO rotational diagrams. In contrast with low-mass protostars, radiative transfer modeling shows that most of CO emission originates from the quiescent envelope (up to 70-100 %), except the highest–J lines that require an additional physical component (shocks). H_2O rotational temperatures are ~250 K, about 100 K higher than for the low-mass protostars due to higher envelope densities and temperatures. Across the wide luminosity range from $\sim$ 1 to 10^6 $L_\odot$, the far-IR line cooling strongly correlates with the bolometric luminosity, in agreement with studies of low-mass protostars, but the relative amount of cooling of hot gas to the dust cooling ratio decreases by more than an order of magnitude from low to high-mass protostars.

Chapter 4 – *Shockingly low water abundances in Herschel / PACS observations of low-mass protostars in Perseus* [WILL]

A large and uniform sample of young protostars (22 objects) located exclusively in the Perseus molecular cloud is observed in selected transitions of H_2O, CO, and OH. Line ratios of the same and different species are used as diagnostics of shocks resulting from the envelope-outflow interactions. Changes in absolute line fluxes and line ratios as a function of shock velocity and pre-shock density are discussed and compared with steady-state non-dissociative and dissociative shocks from the literature. Observed line ratios of the same species are well-reproduced by existing models of non-dissociative *C*−shocks with velocities $\gtrsim$ 20 km s^{-1} and pre-shock densities of $\sim 10^5$ cm^{-3}. In contrast, model line ratios of H_2O / CO, H_2O / OH, and CO / OH are overestimated with respect to the observations by one to two orders of magnitude. The most likely reasons for these discrepancies are too large H_2O abundances and too small OH abundances produced in the shock models. Inclusion of illumination of shocks by ultraviolet radiation from the protostellar environment should allow to reconcile the models with observations.

Chapter 5 – *Physics of deeply-embedded low-mass protostars: evolution of shocks, ultraviolet radiation, and mass loss rates* [WISH, DIGIT, WILL]

A combined survey of 90 low-mass protostars sheds more light on the physical components and their evolution giving rise to the far-infrared emission observed with *Herschel* / PACS. Rich molecular spectra are detected towards 70 out of 90 sources, including ~ 30 sources with the detection of highly-excited H_2O and CO emission. Median CO rotational temperatures are ~ 320 K and ~ 690 K, in line with previous studies. The total cooling in CO decreases as the protostar evolves, but the [O I] emission is surprisingly similar in the Class 0 and I stages. Comparison of [O I] line emission to the shock models implies a necessary contribution from dissociative *J*−shocks and / or UV irradiation of outflow cavities. The [C II] emission, on the other hand, must originate in photodissociation regions, characterized by densities of 10^4 – $10^{5.5}$ cm^{-3} and UV fields of 10-100 times the average interstellar radiation field. The increasing role of UV in the more evolved sources is testified by the decrease of the H_2O / OH ratio from Class 0 to Class I stages. A similar decrease is not seen in the H_2O / [O I] ratio, implying that in Class I sources a large fraction of [O I] emission comes from the H_2O photodissociation in the outflow cavities and not from the jet. As a consequence, the mass loss rates calculated from the [O I] luminosity, of order 10^{-8} $M_\odot$ yr^{-1}, are upper limits to the jet ejection rates. Nevertheless, these rates are up to about an order of magnitude lower than those determined for the entrained outflow gas from the CO 3-2 and CO 6-5 maps, especially for the most deeply embedded sources. In contrast, Class I sources show larger [O I]/CO mass flux rates than the Class 0 sources, suggesting that the jet evolves from molecular to atomic form during the embedded phase.

The main conclusions from this thesis are summarized below.

1. Far-infrared molecular line emission is ubiquitous in star forming regions (Chapters 2-5). 80% of low-mass protostars show detections of CO, H_2O, and OH lines. 40% of those sources show also highly-excited lines of CO and H_2O (Chapter 5).

2. Spatial extent of molecular line emission is typically of order $\sim$ 1000 AU, with a few sources with extended emission up to $\sim 10,000$ AU in the CO outflow direction. The [O I] emission is often extended on the same spatial scales along the outflow direction.

3. Rotational diagrams of CO show uniformly two components in low-mass protostars, corresponding to temperatures of $\sim$ 320 K and $\sim$ 690 K (Chapters 2, 5). The $\sim$300 K component is detected in protostars with a broad range of luminosities, from $\sim$ 1 to 10^6 $L_\odot$ (Chapter 3). Despite the similarities in the CO ladders, the contribution from the envelope to the far-IR CO emission increases 10 times from low- to high-mass protostars (Chapter 3).

4. Evolutionary stage affects the ratio of molecular and atomic cooling more than the mass of a protostar. In contrast, $L_{\rm FIRL}/L_{\rm bol}$ decreases only by a factor of 4 from Class 0 to Class I and more than 20 times from low- to high-mass star forming regions (Chapters 2, 3).

5. Shocks are the main source of hot ($T \gtrsim$300 K) and dense ($n \sim 10^6$ cm^{-3}) gas in low-mass protostars (Chapters 2, 4, 5). Non-dissociative $C-$shocks produce most of the observed molecular emission, but dissociative shocks are needed to explain the [O I] and OH lines as well as the highly-excited CO and H_2O lines (Chapters 4, 5).

6. UV irradiation of shocks needs to be implemented in the next-generation of shock models (Chapters 4, 5). The UV fields are of order 10-100 times the average interstellar radiation field (Chapter 5).

Feedback processes from low- and high-mass star forming regions are therefore successfully identified in the far-IR spectra from *Herschel* / PACS emission. Characteristics of shocks and UV radiation presented here provide additional means to test the origin of protostellar outflows and the launching mechanisms of jets, as well as the scales on which feedback processes occur. Determination of relative jet and UV contributions to the [O I] emission as the protostar evolves is becoming possible with the German REceiver for Astronomy at Terahertz Frequencies (GREAT) instrument on board the Stratospheric Observatory for Infrared Astronomy (SOFIA) which offers [O I] spectroscopy with spectral resolution $\lesssim$1 km s^{-1}.

A complementary view of the feedback processes in the young stellar objects is being provided by sub-millimeter observations with the Atacama Large Millimeter/submillimeter Array (ALMA). Spatially resolved down to $\sim$100 AU scales emission from ^{13}CO $J_{\rm up} < 8$

transitions will fully explore the importance of ultraviolet heating, while, for example, SiO observations will continue to constrain the shock characteristics originating in the outflow-envelope interactions.

High spatial resolution (0.4-0.8") spectral maps from the Mid-Infrared Instrument (MIRI) on the *James Webb Space Telescope* (to be launched in late 2018) will eventually allow us to study hot gas around protostars using the unique mid-IR diagnostics (5-28 μm) on spatial scales similar to ALMA.

Even though *Herschel* is no longer operational, the large amount of data collected in its archives still awaits further exploration. In particular, complete surveys of protostars in nearby molecular clouds will help to develop theoretical models of star formation and protostellar evolution, and their feedback on the surroundings.